CO2 Electrochemical Reduction with Zn-Al Layered Double Hydroxide-Loaded Gas-Diffusion Electrode[†]

OPEN ACCESS

Ryosuke NAKAZATO,[a,*,§] Keeko MATSUMOTO,[a] Noboru YAMAGUCHI,[a] Margherita CAVALLO,[b]
Valentina CROCELLÀ,[b] Francesca BONINO,[b] Matthias QUINTELIER,[c] Joke HADERMANN,[c]
Nataly Carolina ROSERO-NAVARRO,[a,d] Akira MIURA,[a,§] and Kiyoharu TADANAGA[a,*,§§]

[a] *Faculty, Graduate School and School of Engineering, Hokkaido University, Kita 13, Nishi 8, Kita-ku, Sapporo, Hokkaido 060-8628, Japan*
[b] *Department of Chemistry, NIS and INSTM Reference Centers, University of Turin,*
 *Via G. Quarello 15, I-10135 and Via P. Giuria 7, I-10125 Turin, Italy*
[c] *EMAT, Department of Physics, University of Antwerp, Groenenborgerlaan 171, 2020 Antwerp, Belgium*
[d] *Instituto de Cerámica y Vidrio, CSIC, C/Kelsen 5, Campus de Cantoblanco, 28049 Madrid, Spain*

* Corresponding authors: nakazato-ryosuke@eng.hokudai.ac.jp (R. N.), tadanaga@eng.hokudai.ac.jp (K. T.)

ABSTRACT

Carbon dioxide electrochemical reduction (CO_2ER) has attracted considerable attention as a technology to recycle CO_2 into raw materials for chemicals using renewable energies. We recently found that Zn-Al layered double hydroxides (Zn-Al LDH) have the CO-forming CO_2ER activity. However, the activity was only evaluated by using the liquid-phase CO_2ER. In this study, Ni-Al and Ni-Fe LDHs as well as Zn-Al LDH were synthesized using a facile coprecipitation process and the gas-phase CO_2ER with the LDH-loaded gas-diffusion electrode (GDE) was examined. The products were characterized by XRD, STEM-EDX, BF-TEM and ATR-IR spectroscopy. In the ATR-IR results, the interaction of CO_2 with Zn-Al LDH showed a different carbonates evolution with respect to other LDHs, suggesting a

different electrocatalytic activity. The LDH-loaded GDE was prepared by simple drop-casting of a catalyst ink onto carbon paper. For gas-phase CO_2ER, only Zn-Al LDH exhibited the CO_2ER activity for carbon monoxide (CO) formation. By using different potassium salt electrolytes affording neutral to strongly basic conditions, such as KCl, $KHCO_3$ and KOH, the gas-phase CO_2ER with Zn-Al LDH-loaded GDE showed 1.3 to 2.1 times higher partial current density for CO formation than the liquid-phase CO_2ER.
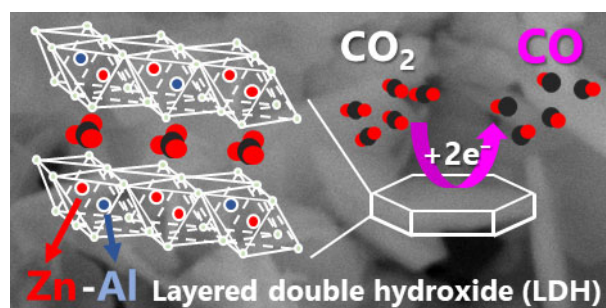
Keywords : CO2 Electrochemical Reduction, CO Formation, Layered Double Hydroxide, Gas-diffusion Electrode

1. Introduction

In recent years, research on carbon dioxide (CO_2) recycling technologies to recycle CO_2 into useful fuel, chemical and polymer precursors or products has attracted considerable attention from a carbon-neutral perspective.[1,2] By using catalysts with highly efficient activity for CO_2 reduction reactions (CO_2RR), CO_2 recycling can be achieved at ambient temperature and pressure.[3] The types of CO_2RR catalysts are classified into photocatalysts, enzyme catalysts, and electrocatalysts. The latter are expected to be promising sustainable CO_2RR catalysts with higher productivity and higher energy conversion efficiency than other catalysts. The CO_2

electrochemical reduction (CO_2ER) using electrocatalysts can use excess electricity generated by renewable energy, such as solar power and wind power, as an energy source.[4] For CO_2 recycling technology, the selectivity of products is an important function. Among various CO_2ER products (carbon monoxide (CO), methane (CH_4), methanol (CH_3OH), formic acid (HCOOH), and C_2 products), CO is an important raw chemical to produce methanol and liquid hydrocarbons.[5] Au, Ag, and Zn-based electrocatalysts are known to perform highly selective CO-forming CO_2ER, but Au and Ag are precious metals. From practical perspectives, electrocatalysts with earth-abundant elements are desired.[6] Zn is the only earth-abundant monometallic electrocatalyst with high CO selectivity, but bulk Zn catalysts tend to show large overpotentials and slow reaction rates due to small numbers of active sites.[7] Monovalent Zn^+ ($3d^{10}4s^1$) has been found to be an active site in many cases due to its coordinatively unsaturated characteristics.[8] For example, it has been reported that Zn catalysts derived from the electrochemical reconstruction of nanostructured ZnO had high CO_2ER activity (91.6 % of CO selectivity at -0.62 V vs. reversible hydrogen electrode (RHE))[9] and that those with more oxidized Zn species (Zn^+) were indicated to be more active (95.3 % of CO selectivity at -1.0 V vs. RHE).[10] Also, the low-crystallinity mesoporous $ZnGa_2O_4$ electrocatalyst, with an abundance of Zn^{2+}/Zn^+ redox

Figure 1. Structure of LDH ($[M^{2+}_{1-x}M^{3+}_x(OH)_2]^{x+}$ $[A^{n-}_{x/n}]^{x-}$).

couples, was reported to show higher activity (96 % of CO selectivity at −0.80 V vs. RHE) than the high-crystallinity one (CO selectivity <37 % at −0.70 to −1.0 V vs. RHE).[11] Thus, precise nanostructure design is required to obtain highly active Zn-based electrocatalysts.

Based on the above findings, zinc oxide (ZnO) and zinc hydroxide ($Zn(OH)_2$) are expected to be promising CO-forming CO_2ER catalysts, but these are not electrochemically stable since the reduction to metal species occurs predominantly at more negative potentials than −0.42 V vs. RHE under pH conditions above 8.[12] Furthermore, the CO-forming CO_2ER involves the formation of hydroxide ions ($OH^−$), as shown in Eq. 1, and tends to be boosted under alkaline conditions.[9,13–15] Thus, the catalysts are required to have high electrochemical stability and alkaline tolerance.

$$CO_2 + H_2O + 2e^- \rightarrow CO + 2OH^- \quad E_o = -0.11 \text{ V vs. RHE}$$
(1)

We focused on layered double hydroxide (LDH), which consists of positively charged metal hydroxide layers and charge-compensating anions (A^{n-}) inserted between the layers. They have the general composition $[M^{2+}_{1-x}M^{3+}_x(OH)_2]^{x+}$ $[A^{n-}_{x/n}]^{x-}$ as shown in Fig. 1, where M^{2+} and M^{3+} are divalent and trivalent metal ions, respectively. Due to the structure, LDHs have characteristics in favour of a CO_2ER catalyst, such as facileness of synthesis,[16–18] diversity of metal composition,[16] large specific surface area,[16] high hydroxide ion conductivity,[17,18] and high alkaline tolerance.[19,20] These properties are also preferable as electrocatalysts for different reactions, so transition metal containing LDHs have been studied as electrocatalysts for oxygen evolution[19–21] and oxygen reduction reactions.[19,20,22] Although various material-based CO_2ER catalysts have been reported, there have been few reports on LDH-based CO_2ER catalysts. To our knowledge, the first study using single-phase LDH as a CO_2ER catalyst was reported in 2022. Cu-Al LDH was shown to be a CO_2ER catalyst forming mainly CO and HCOOH.[23] And then, Cu-Mg-Al LDH was reported to be a CO_2ER catalyst forming mainly acetic acid.[24] In addition, other LDH-based catalysts, which contain metal species or metal complexes as active species, have been investigated for their CO_2ER activity.[25–27] However, among the LDH-based CO_2ER catalysts described above, CO selectivity was not high, at most 42 %.[23] On the other hand, it has been reported that M-Al LDHs (M = Ni, Co)[28] and Zn-M LDHs (M = Al, Ti, Ga)[28,29] exhibited catalytic activity for CO_2 "photo-reduction" with Zn-Al LDH showing the highest CO selectivity (90 %).[29]

The above background motivated a detailed exploration of the CO_2ER activity of LDHs. We found that Zn-Al LDH is a CO-forming CO_2ER catalyst and electrochemically more stable than ZnO, showing a CO selectivity of 77 % with a partial current density for CO formation of 12 mA cm^{-2} under the applied potential of −1.4 V vs. RHE in a potassium bicarbonate ($KHCO_3$) electrolyte solution.[30] However, the reaction treated in that previous study was the liquid-phase CO_2ER as shown in Fig. 2a, and there was a
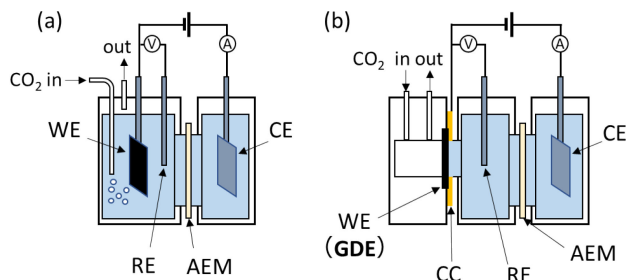
Figure 2. Schematic of a typical CO_2 electrolysis reactor for (a) liquid-phase CO_2ER and (b) gas-phase CO_2ER (GDE: gas diffusion electrode, WE: working electrode, CE: counter electrode, RE: reference electrode, AEM: anion exchange membrane, CC: current collector).

limitation of reaction efficiency because of its common issues, such as low solubility of CO_2 (33.4 mM (M = mol L^{-1})), the slow diffusion rate of ions (1/1000 of that in the air) and electrolyte species limitations.[31] The gas-phase CO_2ER with a gas-diffusion electrode (GDE), as shown in Fig. 2b, is a promising reaction that can overcome such limitations.[31–33] In a GDE, CO_2 is transported in the gas phase and reacts at a thin solid-liquid-gas phase interface. In this process, liquid-phase CO_2 concentration and diffusion do not limit the reaction efficiency, resulting in lower overpotentials and higher current densities for CO_2ER. Furthermore, a strong alkaline electrolyte can be used in the gas-phase CO_2ER since it is not required to dissolve CO_2 into an electrolyte solution.

In the present study, to investigate the potential CO_2ER activity of LDHs, Ni-Al and Ni-Fe LDHs as well as Zn-Al LDH were synthesized using a facile coprecipitation process, and gas-phase CO_2ER with the LDH-loaded GDE was performed. For Zn-Al LDH, gas-phase CO_2ER was conducted using different electrolyte solutions with neutral to strongly basic conditions, where the pH of 1.0 M aqueous electrolyte solutions is 6.5, 8.2 and 14 for potassium chloride (KCl), potassium bicarbonate ($KHCO_3$), and potassium hydroxide (KOH), respectively.

2. Results and Discussion

2.1 Characterization of M^{2+}-M^{3+} LDH (M^{2+} = Zn or Ni, M^{3+} = Al or Fe)

M^{2+}-M^{3+} LDH with CO_3^{2-} anions was prepared using a facile and traditional coprecipitation process as shown in Fig. S1.[34] Figure 3 shows the X-ray diffraction (XRD) patterns and field emission scanning transmission electron microscopy (FE-SEM) image of the synthesized products. As shown in Fig. 3a, the (003) and (006) plane peaks, characteristic of the layered structure, were observed and no impurity peaks were detected in any of the

(a)   (b)
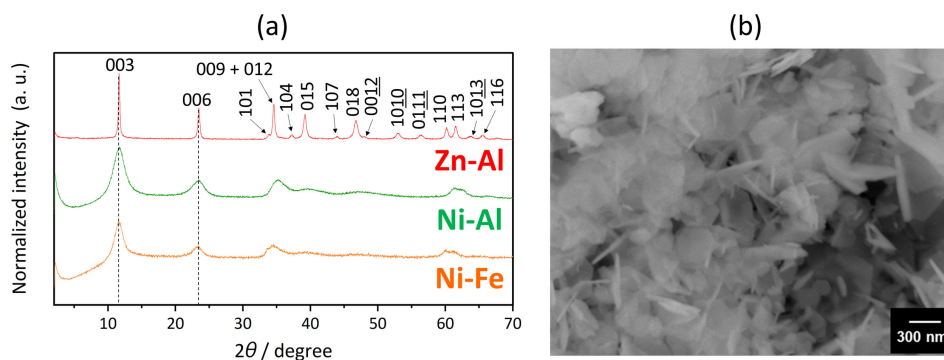
Figure 3. (a) XRD patterns of M^{2+}-M^{3+} LDHs (M^{2+}-M^{3+} = Zn-Al (red line), Ni-Al (green line), or Ni-Fe (orange line)) and (b) FE-SEM image of Zn-Al LDH.

products. Peaks in the Zn-Al system were assigned to the previously reported XRD pattern of Zn-Al LDH with carbonate (CO_3^{2-}) anions as interlayer anions.[34] Similarly, for the Ni-Al and Ni-Fe systems, the formation of LDHs with the interlayer carbonate anions was confirmed.[35,36] However, their peaks were broader than those of Zn-Al LDH, suggesting that the primary grain size was smaller. From the FE-SEM and the bright field transmission electron microscopy (BF-TEM) images, as shown in Figs. 3b and S3a, the plate-like crystals, characteristic of LDH, with a size of one hundred to several hundred nm were observed in Zn-Al LDH. On the other hand, as shown in Figs. S3b and S3c, the BF-TEM images of the Ni-Al and Ni-Fe products showed sub-micron to micron lumped crystals, which were aggregates of fine crystals. The scanning transmission electron microscopy coupled with energy-dispersive X-ray spectrometry (STEM-EDX) mapping showed that elements used as M^{2+} and M^{3+} were homogeneously distributed on the particles in the sub-micron-order as shown in Fig. S3 and the EDX elemental analysis showed the average chemical composition with molar ratios of Zn/Al = 1.96 ± 0.25, Ni/Al = 1.80 ± 0.24 and Ni/Fe = 2.00 ± 0.16 for each product, which is almost the same as the starting composition ratio. These results indicate that all synthesized products are LDH with the formula $[M^{2+}_2M^{3+}_1(OH)_6]^+ [CO_3^{2-}_{0.5}]^-$.

Figure S5 shows the attenuated total reflectance infrared (ATR-IR) spectra of the dry LDHs. The three LDH samples exhibited a common broad band in the high frequency region (3500–2950 cm^{-1}) ascribable to the hydroxyl-stretching vibrations of both structural M-OH species (3500–3400 cm^{-1}) and molecular water present in the interlayer (3300–2950 cm^{-1}).[37] The latter is commonly differentiated between hydrogen-bonded water at around 3300 cm^{-1} and water OH stretching vibrations perturbed by interlayer carbonate anions (2950–3050 cm^{-1}).[37] In the low frequency region, a broad band (1000–650 cm^{-1}) derived from the superimposition of the ν_2 out of plane stretching mode of interlayer carbonate anions (~860 cm^{-1}) and the lattice HO-M-OH and M-OH (M = Zn, Al, Ni, Fe) vibrational modes (450–800 cm^{-1}) was present in all the samples.[38,39] In the intermediate region, a band at 1640 cm^{-1}, which is typical of the bending vibrations of the interlayer water molecules, and an intense peak at around 1350 cm^{-1} with a weak shoulder at ~1410 cm^{-1} due to the ν_3 stretching mode of interlayer carbonate anions were observed.[37] It is worth noting that the ν_3 stretching mode of free carbonate anions is reported to be at 1415 cm^{-1}.[40] However, a change in the symmetry of the molecule could lead to the splitting of the ν_3 in two distinct components at ~1365 and ~1415 cm^{-1}.[41] Additionally, since pre-treatments of the LDHs at high temperature were not be performed to preserve the LDH structure, the additional bands in the 1800–1200 cm^{-1}, partially superimposed to the structural water and carbonates (CO_3^{2-}) signals, are probably related to the formation of surface (non-structural) carbonate species upon the exposure to the CO_2 present in the

atmosphere. In this regard, the Ni-Al and Ni-Fe LDHs interestingly exhibited some additional peaks at 1725 cm^{-1} and 1270 cm^{-1}, which are probably due to the presence of a different family of surface "bridged" carbonate-like species.[40]

In more detail, the difference among the three LDHs upon interaction of CO_2 was investigated by adding CO_2 saturated water on the dry samples (See Figs. S6 and 4 for the 3700–650 cm^{-1} and the 1800–1200 cm^{-1} region, respectively). As shown in Fig. S6, the contact with water caused an increase in the high frequency region bands associated to the OH stretching vibrations together with the increment of the 1640 cm^{-1} signal ascribed to the HOH bending vibrations, while the interaction of CO_2 with basic sites was responsible for the appearance of surface (non-structural) carbonates-like species shown in the 1800–1200 cm^{-1} region. As already mentioned, free carbonate anions generally show a ν_3 asymmetric CO_3^{2-} stretching at around 1415 cm^{-1}, which split in two different signals (the symmetric ν_{3sym} and the asymmetric ν_{3asym} vibrations) when the symmetry is lowered.[40] In addition, when CO_2 interacts with the LDH basic sites, both the symmetric and asymmetric vibrations are detected, and the different carbonate-like species, such as unidentate, bidentate, bridged, and polydentate structures or bicarbonates, formed depending on the type and the strength of the surface sites.[42] To distinguish between carbonates, the most employed criteria is usually based on the $\Delta\nu_3$ splitting even though the frequency of the different species is strongly affected by the structure. The strongest basic sites (unidentate carbonates) are usually associated with the lowest $\Delta\nu_3$ splitting ($\Delta\nu_3 = 100$ cm^{-1}), followed by basic sites of medium strength (bidentate carbonates) ($\Delta\nu_3 = 300$ cm^{-1}) and by weak basic sites (bridged species) ($\Delta\nu_3 = 400$ cm^{-1}).[43] However, the appearance of those species on the different LDHs fell in the region deriving from the HOH bending vibration of water (~1640 cm^{-1}) and the interlayer carbonates anions (~1350 and 1410 cm^{-1}), whose intense bands strongly affect the identification of surface carbonate species (See Figs. S6 and 4a, 4b and 4c). For this reason, the identification of the main spectral change occurring in the carbonate region upon CO_2 contact is possible just by subtracting the spectra of the corresponding wet N_2-saturated samples (See Figs. 4d, 4e, and 4f). For all LDHs, the CO_2 contact was responsible for the increase of the intense band at around 1610 cm^{-1}, which shifted to different wavenumbers depending on the kind of LDHs (1606 cm^{-1} for Ni-Fe, 1613 cm^{-1} for Ni-Al and 1623 cm^{-1} for Zn-Al), and the simultaneous decrease of the signal at 1360 cm^{-1}. However, the Ni-Al and Ni-Fe LDHs behave differently compared to Zn-Al one in the remaining spectral regions. In particular, upon CO_2 contact, the Ni-Al and Ni-Fe LDHs exhibit two broad and intense bands at ~1500 cm^{-1} and at ~1295 cm^{-1}, which are nearly absent in the Zn-Al one. Additionally, the decrease of the band at 1360 cm^{-1} occurs simultaneously to the component at around 1420 cm^{-1}, which is located at different frequencies in

3
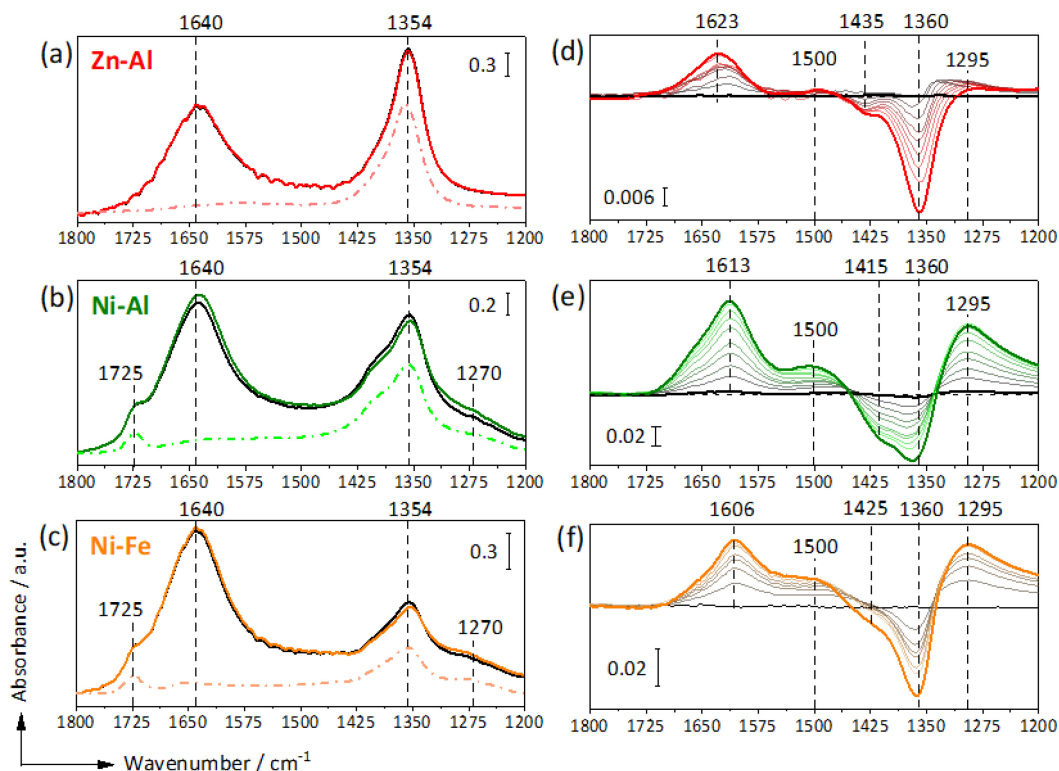
Figure 4. In-situ ATR-IR spectra in the carbonate-like region (1800–1200 cm^{-1}) of: Zn-Al LDH (a), Ni-Al LDH (b) and Ni-Fe LDH (c). The corresponding differential spectra (obtained by subtracting the spectra of the wet N_2-saturated sample to that of the wet CO_2-saturated sample) are shown on the right side (d–f). Dotted colored, black, and continuous colored curves represent the dry, wet N_2-saturated, and wet CO_2-saturated samples, respectively. The curves of intermediate CO_2 coverage are shown in grey. In adsorption differential spectral patterns (d–f), the bands relative to species that form or increase upon CO_2 contact are pointing up, bands relative to species that decrease are pointing down.

the three LDHs: 1415 cm^{-1} in Ni-Al, 1425 cm^{-1} in Ni-Fe and 1435 cm^{-1} in Zn-Al. Finally, the bands at 1725 cm^{-1} and 1270 cm^{-1} which are originally present in the Ni-Al and Ni-Fe LDHs and assigned to surface "bridged" carbonates were not changed by CO_2 contact, suggesting the stability of these carbonate species in the as-synthesized LDHs (See Figs. 4b and 4c and corresponding differential spectra 4e and 4f). A correct assignment of the carbonate species formed upon CO_2 adsorption is not straightforward for at least two reasons: the superposition of the signals generated by structural carbonate and water molecule and the possible loss of a fraction of deposited sample during the experiment. However, based on the $\Delta\nu_3$ splitting ($\Delta\nu_3 > 100$), the formation of bidentate species likely occurs. Additionally, the presence of bicarbonates is highly unlikely due to the absence of the characteristic sharp band at ~1220 cm^{-1} associated to the COH bending mode.[40,44] The differences in the spectra of Ni-Al, Ni-Fe and Zn-Al show the formation of different families of bidentate carbonates with different strength and stability, which also suggests the presence of different basic sites in the tree LDHs. These differences could affect the reaction processes such as intermediate formation steps and CO desorption step, and by extension, could lead to different catalytic behaviors in the tree LDHs.

2.2 Gas-phase CO_2ER with LDH-loaded GDE in 1.0 M aqueous KHCO$_3$ solution

Gas-phase CO_2ER with the LDH-loaded GDE was carried out by using a custom-made three-electrode setup composed of a three-compartment cell as shown in Fig. S2. The LDH-loaded GDE was prepared by simple drop-casting of the catalyst ink on a carbon sheet with gas-diffusion layer (GDL) as shown in Fig. S7, which

exhibited the cross-sectional SEM image and EDX mapping of Zn for the Zn-Al LDH-loaded GDE. A 1.0 M aqueous KHCO$_3$ solution was used as the typical electrolyte. The applied potential dependence of Faradaic efficiency (*FE*) and current density (*j*) for the cathodes with or without LDHs are shown in Figs. 5 and S8, respectively. Electrode potentials in the study were converted to the reversible hydrogen electrode (RHE) or the standard hydrogen electrode (SHE) according to the following equations: $E_{RHE} = E_{SHE} + 0.059 \times$ pH, $\quad E_{SHE} = E_{Ag/AgCl} + 0.222$ V $= E_{Hg/HgO} + 1.760$ V.

As shown in Fig. S8, for all cathodes, the current density increased with more negative applied potentials, and catalytic currents were observed. Focusing on *FE* of the cathode with Zn-Al LDH, as shown in Fig. 5a, CO formation was dominated at more negative applied potentials than -1.0 V vs. RHE, with 59 % of the *FE* at -1.0 V vs. RHE and the highest *FE* of 67 % was shown at -1.4 and -1.8 V vs. RHE. At the same applied potential, H_2 formation was observed as a major side-reaction with more than 20 % of the *FE*, and electron consumption by other reactions gave less than 10 % of the *FE*. On the other hand, in *FE* of the cathode with Ni-Al LDH, Ni-Fe LDH, or without LDH, H_2 formation was dominated as shown in Figs. 5b, 5c and 5d, respectively. Therefore, it was suggested that only Zn-Al LDH acts as a CO_2ER catalyst. Methane (CH$_4$) was detected as a minor product, but its *FE* was less than 0.1 % for all cathodes. Then, trace amount of formic acid (HCOOH) was detected as the only liquid product, but its concentration is under the limit of quantification. Thus, the *FE* for CO and H_2 are discussed in this study.

Regarding the stability of Zn-Al LDH during CO_2ER, a constant current density at all applied potentials was observed for 10 min of
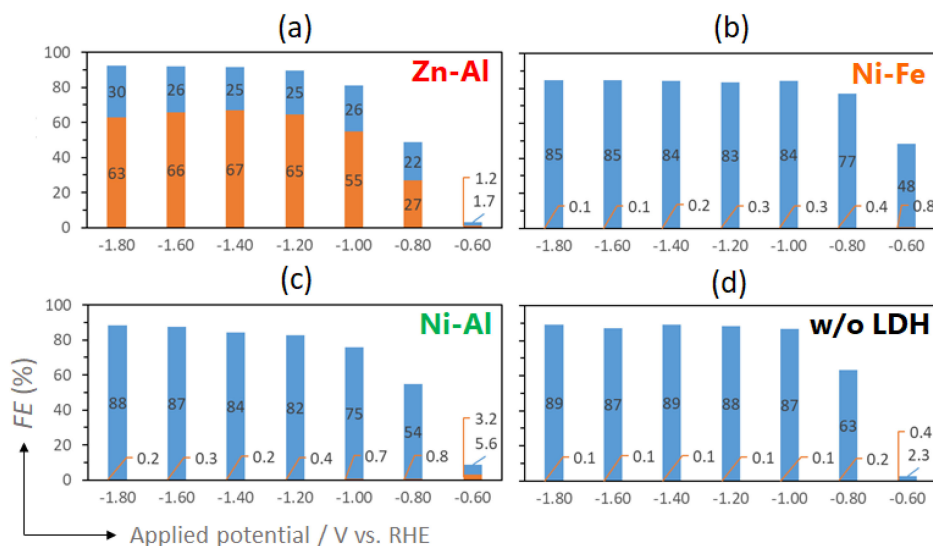
Figure 5. Applied potential dependence of Faradaic efficiency (*FE*) for CO_2ER in 1.0 M aqueous $KHCO_3$ solution using each cathode with (a) Zn-Al LDH, (b) Ni-Fe LDH and (c) Ni-Al LDH, and (d) without LDH. (orange bar: CO, blue bar: H_2)

total reaction time in the chronoamperogram as shown in Fig. S9, and the SEM-EDX elemental analysis for the surface of Zn-Al LDH-loaded GDE showed almost no change in the average chemical compositions with the molar ratio of Zn/Al before and after electrolysis, which were 1.92 ± 0.16 and 2.02 ± 0.17, respectively. In addition, the turnover number (*TON*) of these reactions, assuming one Zn atom as the active site, were 0.90, 2.0, 3.1, 4.2 and 5.2 at -1.0, -1.2, -1.4, -1.6 and -1.8 V vs. RHE, respectively. Thus, the *TON* above 1 was gained, indicating that Zn-Al LDH exhibits CO-selective electrocatalytic activity in gas-phase CO_2ER.

Interestingly, the Ni-Al and Ni-Fe LDHs which show the lowest CO evolution also exhibit a different carbonates evolution upon CO_2 adsorption. The accordance of the CO_2ER activity with the in-situ ATR-IR spectroscopy supports the hypothesis that the different carbonates formed in Zn-Al LDH are responsible for a higher CO_2ER activity.

### 2.3 Gas-phase CO_2ER with LDH-loaded GDE in different electrolytes

To investigate the potential CO_2ER activity of Zn-Al LDH, the gas-phase CO_2ER activities of Zn-Al LDH under neutral to strong basic conditions (pH of 1.0 M aqueous electrolyte solutions: 6.5 for KCl, 8.2 for $KHCO_3$, 14 for KOH) were compared. Although KOH cannot be used as an electrolyte in liquid-phase CO_2ER because it forms carbonate salts with dissolved CO_2 in an electrolyte solution, it is known that the gas-phase CO_2ER with Ag and Au nanoparticle catalysts was boosted under strong alkaline conditions than the neutral condition: a strong alkaline condition causes lower over-potential and higher current density and *FE*.[14,15,45]

Figures 6, S10, S11 and S12 show the applied potential dependence of current density (j) and *FE* for CO_2ER with Zn-Al LDH in each 1.0 M aqueous solution of KCl, $KHCO_3$, and KOH. As shown in Fig. 5 (upper row), as the pH of electrolytes increased, the onset potentials for the partial current density of CO formation (j_{CO}) decreased (KCl: 0.90 V vs. RHE, $KHCO_3$: 0.80 V vs. RHE, KOH: 0.50 V vs. RHE), and the maximum $|j_{CO}|$ for the KOH electrolyte (25 mA cm^{-2}) was higher than that for the KCl and $KHCO_3$ (17 mA cm^{-2} and 15 mA cm^{-2}, respectively). However, the $|j_{CO}|$ for all electrolytes was less than 30 mA cm^{-2} even at relatively negative potentials and, as the pH of electrolytes increased, the maximum *FE* of CO (FE_{CO}) decreased (KCl: 69 %, $KHCO_3$: 67 %,

KOH: 64 %), as shown in Figs. 6c, S10a, S11a and S12a. Since a trace amount of formic acid was also detected but no other products were detected in the KCl and KOH conditions as well as in the $KHCO_3$ condition, the main cause of the slight decrease in FE_{CO} with increasing the pH of electrolytes could be the loss of CO by dissolution into the electrolyte, which is more likely to occur in alkaline electrolytes.

The effect of electrolyte type on the CO_2ER activity of Zn-Al LDH was studied in more detail using the Tafel analysis. As shown in Fig. S13a, the Tafel behavior of the j_{CO} plotted with over-potentials showed that the slopes were almost identical for all electrolytes (KCl: 121 mV dec^{-1}, $KHCO_3$: 140 mV dec^{-1}, KOH: 115 mV dec^{-1}). Furthermore, the near overlap was observed in the Tafel plots converted with the applied potential vs. standard hydrogen electrode (SHE) for all electrolytes as shown in Fig. S13c, indicating that the rate-determining step (RDS) was not affected by pH of the bulk solution. This behavior is consistent with the previously reported behaviors for Ag and Au nanoparticle catalysts,[45] deriving from the phenomenon that the local pH of the cathode surface under CO-forming CO_2ER remains basic (pH > 8) even under the KCl condition.[9,15] Therefore, the CO_2ER by Zn-Al LDH is also considered to depend on the local pH of the cathode surface.

Table S1 showed the summary of $|j_{CO}|$ and FE_{CO} in the case of gas-phase and liquid-phase CO_2ER by Zn-Al LDH. As expected, it was revealed that the gas-phase CO_2ER showed 1.4, 1.3, and 2.1 times higher $|j_{CO}|$ than the liquid-phase CO_2ER at -1.4 V vs. RHE for KCl, $KHCO_3$, and KOH, respectively. However, these increases of $|j_{CO}|$ were not as much as a typical gas-phase CO_2ER, since gas-phase CO_2ER by highly active catalysts such as Ag and Au nanoparticle was reported to give the current density of 100 mA cm^{-2} or more.[33] The low $|j_{CO}|$ in the case of gas-phase CO_2ER by Zn-Al LDH could be derived from high overpotential due to the low electrical conductivity,[28] low stability of the key $CO_2^{\cdot-}$ intermediate (one-electron-reduced CO_2 state), the high affinity for CO_2, or the high basicity of LDH. Considering that the Tafel slope for Zn-Al LDH was comparable to that for Ag and Au nanoparticle catalysts (110 to 230 mV dec^{-1}),[15,45] Theoretically, a Tafel slope of 118 mV dec^{-1} means that RDS is the first one-electron transfer to CO_2, while a Tafel slope of 59 mV dec^{-1} implies that RDS is a chemical reaction occurring after the first one-electron reduction of CO_2.[11,46] The Tafel slopes for Zn-Al LDH for all
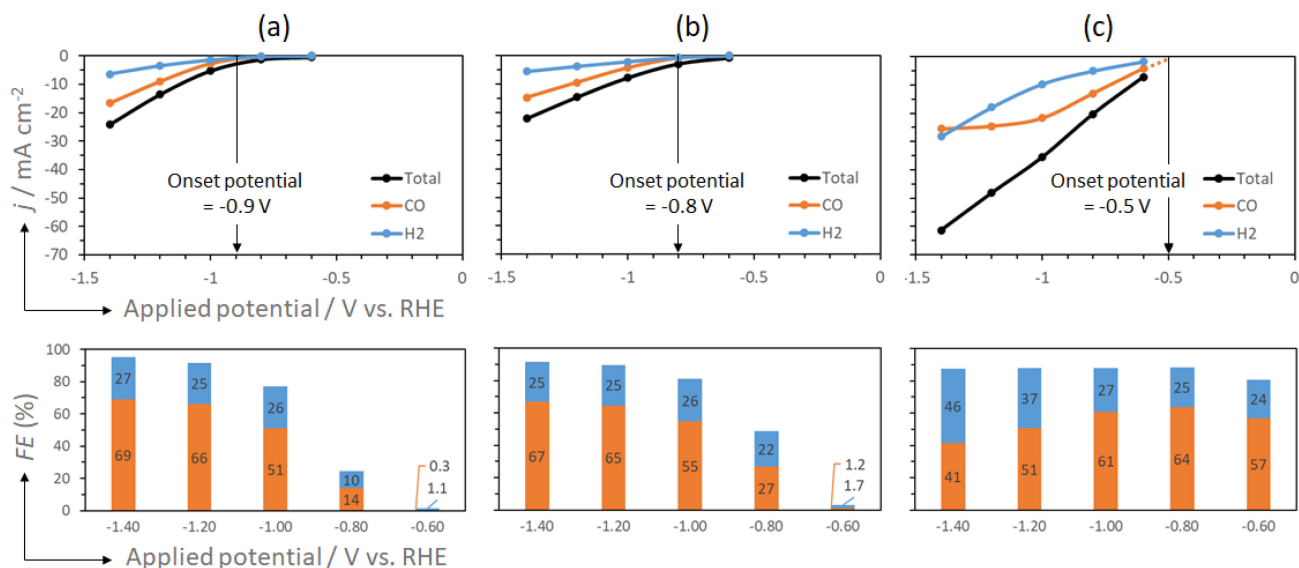
Figure 6. Applied potential dependence of current density (j), onset potentials for the partial current density of CO formation (upper row figures) and Faradaic efficiency (*FE*, lower row figures; orange bar: CO, blue bar: H_2) for CO_2ER with Zn-Al LDH in each 1.0 M aqueous solution of (a) KCl, (b) $KHCO_3$ and (c) KOH.

electrolytes were comparable to 118 mV dec^{-1}, indicating that the first one-electron transfer reaction to CO_2 was RDS regardless of the types of electrolytes, and the low electrical conductivity or low stability of the key $CO_2^{\cdot-}$ intermediate of Zn-Al LDH caused the low $|j_{CO}|$. On the other hand, the high affinity for CO_2 or the high basicity of LDH could cause the slow diffusion of CO_2 or proton donors onto the LDH surface, leading to the limitation of $|j_{CO}|$ at the high overpotential. As shown in Fig. S13b, when the overpotential increased beyond the electron transfer rate-determining range, the Tafel plot curved and the current density saturated at a certain value (approximately 30 mA cm^{-2}) for all electrolyte types, suggesting the existence of a slow RDS in the mass transport process.

Regarding the stability of Zn-Al LDH during CO_2ER under the KCl and KOH electrolytes, a constant current density at all applied potential was observed for 10 min of total reaction time in the chronoamperogram as shown in Fig. S14. However, the longer-term stability test has not been studied because of leaks of electrolyte solution into the gas-phase chamber about 1 hour after starting the reaction. While this problem has been reported to be solved by adjusting the CO_2 supply pressure,[47] it can also be solved by using a membrane electrode assembly (MEA).[48,49] Reaction cells using MEAs are called zero-gap cells, where the cell voltage can be minimized by direct contact of GDE with a polymer electrolyte membrane without electrolyte solution in between. Because the zero-gap cell is the most practical reaction system, the application of Zn-Al LDH for MEAs could be a promising future challenge.

3. Conclusions

Gase-phase CO_2ER activity of M^{2+}-M^{3+} LDH was studied using Ni-Al, Ni-Fe or Zn-Al LDHs. The in-situ ATR-IR measurements highlighted that the three LDH samples formed, upon CO_2 adsorption, different families of bidentate carbonates with different strength and stability which are leading to a different reactivity of the samples. The Zn-Al LDH, which showed a different carbonate evolution in in-situ ATR-IR measurements, exhibited the highest CO-forming CO_2ER activity. By using different potassium salt electrolytes affording neutral to strongly basic conditions, such as KCl, $KHCO_3$ and KOH, the gas-phase CO_2ER with Zn-Al LDH-loaded GDE showed 1.3 to 2.1 times higher partial current density

for CO formation than the liquid-phase CO_2ER. However, the general advantages expected in the gas-phase CO_2ER did not seem to work effectively for CO_2ER by Zn-Al LDH. From the above results, the following prospects are expected to lead to the further development of Zn-Al LDH as a CO_2ER catalyst: control of Zn-Al LDH particle size and exfoliation of laminated Zn-Al LDH for the optimization of its electronic conductivity, affinity for CO_2, and the high basicity.

CRediT Authorship Contribution Statement

Ryosuke Nakazato: Formal analysis (Lead), Investigation (Lead), Visualization (Lead), Writing – original draft (Lead)
Keeko Matsumoto: Investigation (Supporting), Visualization (Supporting)
Noboru Yamaguchi: Investigation (Supporting)
Margherita Cavallo: Formal analysis (Supporting), Investigation (Supporting), Visualization (Supporting)
Valentina Crocellà: Formal analysis (Supporting), Investigation (Supporting), Visualization (Supporting)
Francesca Bonino: Writing – review & editing (Supporting)
Matthias Quintelier: Investigation (Supporting), Visualization (Supporting), Writing – review & editing (Supporting)
Joke Hadermann: Writing – review & editing (Supporting)
Nataly Carolina Rosero-Navarro: Funding acquisition (Supporting), Writing – review & editing (Supporting)
Akira Miura: Writing – review & editing (Supporting)
Kiyoharu Tadanaga: Conceptualization (Lead), Funding acquisition (Lead), Writing – review & editing (Lead)

Data Availability Statement

The data that support the findings of this study are openly available under the terms

of the designated Creative Commons License in J-STAGE Data listed in D1 of References.

Conflict of Interest

The authors declare no conflict of interest in the manuscript.

Funding

References

D1. R. Nakazato, K. Matsumoto, N. Yamaguchi, M. Cavallo, V. Crocellà, F. Bonino, M. Quintelier, J. Hadermann, N. C. Rosero-Navarro, A. Miura, and K. Tadanaga, *J-STAGE Data*, https://doi.org/10.50892/data.electrochemistry.24069993, (2023).

1. A. Tatin, J. Bonin, and M. Robert, *ACS Energy Lett.*, **1**, 1062 (2016).
2. P. De Luna, C. Hahn, D. Higgins, S. A. Jaffer, T. F. Jaramillo, and E. H. Sargent, *Science*, **364**, eaav3506 (2019).
3. J. Qiao, Y. Liu, F. Hong, and J. Zhang, *Chem. Soc. Rev.*, **43**, 631 (2014).
4. K. Kamiya, K. Fujii, M. Sugiyama, and S. Nakanishi, *Chem. Lett.*, **50**, 166 (2021).
5. J. M. Spurgeon and B. Kumar, *Energy Environ. Sci.*, **11**, 1536 (2018).
6. X. Zhang, S.-X. Guo, K. A. Gandionco, A. M. Bond, and J. Zhang, *Mater. Today Adv.*, **7**, 100074 (2020).
7. Y. Hori, H. Wakebe, T. Tsukamoto, and O. Koga, *Electrochim. Acta*, **39**, 1833 (1994).
8. G. Chen, Y. Zhao, L. Shang, G. I. N. Waterhouse, X. Kang, L. Wu, C. Tung, and T. Zhang, *Adv. Sci.*, **3**, 1500424 (2016).
9. W. Luo, Q. Zhang, J. Zhang, E. Moioli, K. Zhao, and A. Züttel, *Appl. Catal., B*, **273**, 119060 (2020).
10. D. L. T. Nguyen, M. S. Jee, D. H. Won, H. Jung, H. S. Oh, B. K. Min, and Y. J. Hwang, *ACS Sustainable Chem. Eng.*, **5**, 11377 (2017).
11. M. Zhao, Y. Gu, P. Chen, Z. Xin, H. Zhu, B. Wang, K. Zhu, S. Yan, and Z. Zou, *J. Mater. Chem. A*, **7**, 9316 (2019).
12. A. R. Mainar, O. Leonet, M. Bengoechea, I. Boyano, I. de Meatza, A. Kvasha, A. Guerfi, and J. Alberto Blázquez, *Int. J. Energy Res.*, **40**, 1032 (2016).
13. C. Shen, L. Liu, J. Ma, J. Zhou, S. Zhang, H. Cheng, Y. Ge, T. Zhang, Z. Tong, and B. Zhang, *J. Mater. Sci.*, **55**, 11714 (2020).
14. K. Torbensen, C. Han, B. Boudy, N. von Wolff, C. Bertail, W. Braun, and M. Robert, *Chem. Eur. J.*, **26**, 3034 (2020).
15. S. Verma, Y. Hamasaki, C. Kim, W. Huang, S. Lu, H. R. M. Jhong, A. A. Gewirth, T. Fujigaya, N. Nakashima, and P. J. A. Kenis, *ACS Energy Lett.*, **3**, 193 (2018).
16. C. I. Ezeh, M. Tomatis, X. Yang, J. He, and C. Sun, *Ultrason. Sonochem.*, **40**, 341 (2018).
17. D. Kubo, K. Igarashi, S. Ishiyama, N. C. Rosero Navarro, A. Miura, M. Higuchi, and K. Tadanaga, *J. Ceram. Soc. Jpn.*, **127**, 788 (2019).
18. K. Tadanaga, Y. Furukawa, A. Hayashi, and M. Tatsumisago, *Adv. Mater.*, **22**, 4401 (2010).
19. H. Kowsari, M. Mehrpooya, and F. Pourfayaz, *Int. J. Hydrogen Energy*, **45**, 27129 (2020).
20. L. Lu, Y. Zheng, R. Yang, A. Kakimov, and X. Li, *Mater. Today Chem.*, **21**, 100488 (2021).
21. Y. Arishige, D. Kubo, K. Tadanaga, A. Hayashi, and M. Tatsumisago, *Solid State Ionics*, **262**, 238 (2014).
22. Y. Iwai, A. Miura, N. C. Rosero-Navarro, M. Higuchi, and K. Tadanaga, *J. Asian Ceram. Soc.*, **7**, 147 (2019).
23. K. Iwase, T. Hirano, and I. Honma, *ChemSusChem*, **15**, e202102340 (2022).
24. M. Serafini, F. Mariani, A. Fasolini, E. T. Brandi, E. Scavetta, F. Basile, and D. Tonelli, *Adv. Funct. Mater.*, **33**, 2300345 (2023).
25. N. Altaf, S. Liang, R. Iqbal, M. Hayat, T. R. Reina, and Q. Wang, *J. CO$_2$ Util.*, **40**, 101205 (2020).
26. N. Altaf, S. Liang, L. Huang, and Q. Wang, *J. Energy Chem.*, **48**, 169 (2020).
27. A. Tarhini, J. Aguirre-Araque, M. Guyot, C. Costentin, G. Rogez, S. Chardon-Noblat, V. Prevot, and C. Mousty, *Electrocatalysis*, **14**, 111 (2023).
28. S. Bai, Z. Wang, L. Tan, G. I. N. Waterhouse, Y. Zhao, and Y. F. Song, *Ind. Eng. Chem. Res.*, **59**, 5848 (2020).
29. X. Xiong, Y. Zhao, R. Shi, W. Yin, Y. Zhao, G. I. N. Waterhouse, and T. Zhang, *Sci. Bull.*, **65**, 987 (2020).
30. N. Yamaguchi, R. Nakazato, K. Matsumoto, M. Kakesu, N. C. Rosero-Navarro, A. Miura, and K. Tadanaga, *J. Asian Ceram. Soc.*, **11**, 406 (2023).
31. D. M. Weekes, D. A. Salvatore, A. Reyes, A. Huang, and C. P. Berlinguette, *Acc. Chem. Res.*, **51**, 910 (2018).
32. S. Hernandez-Aldave and E. Andreoli, *Catalysts*, **10**, 713 (2020).
33. J. Song, H. Song, B. Kim, and J. Oh, *Catalysts*, **9**, 224 (2019).
34. M. Yasaei, M. Khakbiz, A. Zamanian, and E. Ghasemi, *Mater. Sci. Eng., C*, **103**, 109816 (2019).
35. Y. Liu, T. Yu, R. Cai, Y. Li, W. Yang, and J. Caro, *RSC Adv.*, **5**, 29552 (2015).
36. X. Long, J. Li, S. Xiao, K. Yan, Z. Wang, H. Chen, and S. Yang, *Angew. Chem.*, **126**, 7714 (2014).
37. J. T. Kloprogge and R. L. Frost, *J. Solid State Chem.*, **146**, 506 (1999).
38. E. Alibakhshi, E. Ghasemi, M. Mahdavian, and B. Ramezanzadeh, *Prog. Color. Color. Coatings*, **9**, 233 (2016).
39. J. Liu, J. Song, H. Xiao, L. Zhang, Y. Qin, D. Liu, W. Hou, and N. Du, *Powder Technol.*, **253**, 41 (2014).
40. G. Busca and V. Lorenzelli, *Mater. Chem.*, **7**, 89 (1982).
41. F. M. Labajos, V. Rives, and M. A. Ulibarri, *Spectrosc. Lett.*, **24**, 499 (1991).
42. K. Coenen, F. Gallucci, B. Mezari, E. Hensen, and M. van Sint Annaland, *J. CO$_2$ Util.*, **24**, 228 (2018).
43. D. P. Debecker, E. M. Gaigneaux, and G. Busca, *Chem. Eur. J.*, **15**, 3920 (2009).
44. R. Philipp and K. Fujimoto, *J. Phys. Chem.*, **96**, 9035 (1992).
45. W.-H. Cheng, M. H. Richter, I. Sullivan, D. M. Larson, C. Xiang, B. S. Brunschwig, and H. A. Atwater, *ACS Energy Lett.*, **5**, 470 (2020).
46. D. D. Zhu, J. L. Liu, and S. Z. Qiao, *Adv. Mater.*, **28**, 3423 (2016).
47. P. Jeanty, C. Scherer, E. Magori, K. Wiesner-Fleischer, O. Hinrichsen, and M. Fleischer, *J. CO$_2$ Util.*, **24**, 454 (2018).
48. X. Wu, J. W. Sun, P. F. Liu, J. Y. Zhao, Y. Liu, L. Guo, S. Dai, H. G. Yang, and H. Zhao, *Adv. Funct. Mater.*, **32**, 2107301 (2022).
49. R. Lin, J. Guo, X. Li, P. Patel, and A. Seifitokaldani, *Catalysts*, **10**, 473 (2020).